

## FULL EULERIAN FINITE ELEMENT ANALYSIS OF PRESSURE-SENSITIVE ADHESIVES

K. Nishiguchi<sup>1,2</sup>, K. Maeda<sup>1</sup>, S. Okazawa<sup>2</sup>

<sup>1</sup> Functional Design Technology Center, Nitto Denko Corporation, Japan  
([koji\\_nishiguchi@gg.nitto.co.jp](mailto:koji_nishiguchi@gg.nitto.co.jp))

<sup>2</sup> Department of Transportation and Environmental Systems, Hiroshima University, Japan

**Abstract.** *This paper presents a novel simulation method for the large deformation behavior of pressure-sensitive adhesives (PSAs). The focus is on visco-hyperelasticity and temperature-dependence of PSAs. All the basic equations are numerically solved in the Eulerian framework because it allows arbitrarily large deformations. Visco-hyperelasticity is formulated using Simo's finite-strain viscoelastic model, where hyperelasticity is modeled as a novel strain energy function of the left Cauchy-Green deformation tensor. The left Cauchy-Green deformation tensor is temporally updated from the Eulerian velocity field. Temperature-dependence is described with the time-temperature superposition principle of Williams, Landel, and Ferry. To validate the proposed approach, we simulate uniaxial tension tests under different tensile speed and temperature conditions.*

**Keywords:** *Eulerian formulation, Large deformation, Hyperelasticity, Adhesive.*

### 1. INTRODUCTION

In recent years, pressure-sensitive adhesives (PSAs) have been increasingly used in various industrial fields, from automobiles and building materials to electronic devices and transdermal drug delivery systems. This widespread use of PSAs is due to ease of application and technological advances. In the literature, many experimental studies of PSAs have been presented. At the same time, there has been a growing need for numerical simulations of the performance gain of PSAs. Numerical simulations, however, have not been practically used to design the structural and material properties of PSAs for two reasons. The first one is the difficulty of simulations of extremely large deformation and failure that tend to occur in industrial applications of PSAs. Fig.1 shows peeling behavior of a PSA sheet. As shown in Fig.1, the PSA shows large deformation with cohesive and interfacial failure [1, 2]. Such deformations cannot be simulated with a Lagrangian finite element method due to highly distorted elements. The second reason is that PSAs exhibit strong material nonlinearity such as viscosity, hyperelasticity, temperature-dependence, failure, and chemical interfacial force

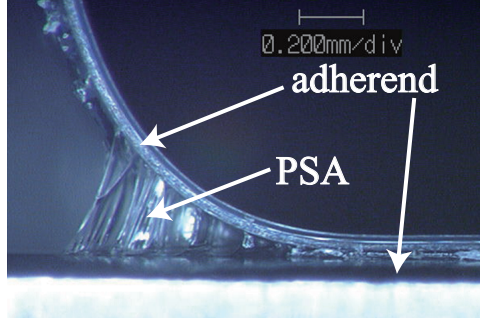


Figure 1. Stringiness phenomenon in peel test.

between adherend and adhesive [3]. A constitutive model for such phenomena has not been presented in the literature.

Recently, we proposed a visco-hyperelastic analysis scheme [4] based on Eulerian finite element method [5] for the dynamics of PSAs. An Eulerian finite element method can treat arbitrarily large deformations and create new free surfaces in a natural manner in the spatially-fixed mesh [5]. In this paper, we propose the temperature-dependent visco-hyperelastic formulation based on an Eulerian finite element method. The paper is organized as follows. In Section 2, we present the basic equations and formulate the constitutive equation in the Eulerian framework. In Section 3, we explain the numerical algorithm in terms of an Eulerian/ALE finite element method. In Section 4, to validate the proposed approach, we simulate uniaxial tension tests under different tensile speed and temperature conditions. In Section 5, conclusions are drawn.

## 2. BASIC EQUATIONS

PSAs are usually based on an elastomer compounded with a suitable tackifier. In this study, PSAs are modeled as macroscopic systems described with the continuum theory because a microscopic approach tends to become too complicated to yield the desired results and therefore doesn't meet our present needs.

### 2.1. Equation of motion and boundary conditions

Let  $\Omega \subset R^{n_{\text{dim}}}$  ( $n_{\text{dim}}=1,2$ , or 3) be the current configuration of a continuum body with a smooth boundary  $\Gamma = \partial\Omega$  as shown in Fig.2, where  $\mathbf{v}$  is the velocity vector,  $\mathbf{b}$  is the body force per unit mass,  $\mathbf{t}$  is the Cauchy traction vector, and the overline indicates a given quantity. Derived from the momentum conservation law, the equation of motion for the current configuration of the body in the Eulerian description is given by

$$\rho \left\{ \frac{\partial \mathbf{v}}{\partial t} + (\mathbf{v} \cdot \nabla) \mathbf{v} \right\} = \nabla \cdot \boldsymbol{\sigma} + \rho \mathbf{b}, \quad (1)$$

where  $\rho$  is the current mass density,  $\boldsymbol{\sigma}$  is the Cauchy stress tensor, and  $\partial/\partial t$  is the spatial time derivative. In addition, both the kinematic and dynamic boundary conditions are defined as

$$\mathbf{v} = \overline{\mathbf{v}}, \quad (2)$$

$$\boldsymbol{\sigma} \cdot \mathbf{n} = \bar{\mathbf{t}}, \quad (3)$$

respectively on  $\Gamma_v \cup \Gamma_t = \partial\Omega$ . Here,  $\mathbf{n}$  is the outward unit normal vector on the boundary surface  $\partial\Omega$  in the current configuration.

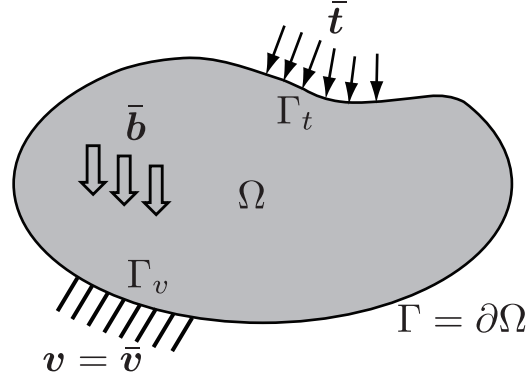


Figure 2. Moving solid body in the current configuration.

## 2.2. Deformation measure in the Eulerian framework

In the Lagrangian framework, solid deformation is described using the deformation gradient tensor

$$\mathbf{F} = \frac{\partial \mathbf{x}}{\partial \mathbf{X}}, \quad (4)$$

where  $\mathbf{x}$  is the current position vector of material points while  $\mathbf{X}$  is the referential position vector. By contrast, the Eulerian description lacks material points to link the reference and current configurations. Therefore, we must devise a method to describe solid deformation without material points. To this end, we introduce the material time derivative of the left Cauchy-Green deformation tensor. The left Cauchy-Green deformation tensor is defined by

$$\mathbf{B} = \mathbf{F} \cdot \mathbf{F}^T. \quad (5)$$

According to the definition (5) and the product rule, we obtain

$$\frac{D\mathbf{B}}{Dt} = \frac{D(\mathbf{F} \cdot \mathbf{F}^T)}{Dt} \quad (6)$$

$$= \frac{D\mathbf{F}}{Dt} \cdot \mathbf{F}^T + \mathbf{F} \cdot \frac{D\mathbf{F}^T}{Dt}, \quad (7)$$

where  $D/Dt$  is the material time derivative. We then find the useful relationship

$$\frac{\partial \mathbf{B}}{\partial t} + (\mathbf{v} \cdot \nabla) \mathbf{B} = \mathbf{L} \cdot \mathbf{B} + \mathbf{B} \cdot \mathbf{L}^T \quad (8)$$

with the relation  $D\mathbf{F}/Dt = \mathbf{L} \cdot \mathbf{F}$ . Here,  $\mathbf{L}$  is the spatial velocity gradient, which is defined by  $\mathbf{L} = \nabla \mathbf{v}$ . For the stress-free reference configuration, the left Cauchy-Green deformation tensor must satisfy the initial condition, i.e.  $\mathbf{B} = \mathbf{I}$ . According to the relation (8), the left Cauchy-Green deformation tensor is temporally updated from the Eulerian velocity field without material points.

### 2.3. Constitutive equation for temperature-dependent visco-hyperelasticity

PSAs can sustain finite strains without noticeable volume changes and be regarded as initially isotropic material. In this paper, we postulate that PSAs are incompressible isotropic material and focus on the viscosity, hyperelasticity, and temperature-dependence.

To describe the temperature-dependence, we introduce the time-temperature superposition principle, which is frequently used to describe the mechanical relaxation behaviour of polymers. According to this principle, time and temperature are equivalent, i.e. a given property measured for short times at a given temperature is identical with one measured for longer times at a lower temperature. In order to convert the experimental relaxation time  $\tau$  at a measured temperature  $\theta$  into the equivalent relaxation time  $\tau'$  at a reference temperature  $\theta_r$ , the shift factor  $a(\theta)$  is defined by

$$\tau' = \frac{\tau}{a(\theta)} . \quad (9)$$

In the literature various functional forms of the shift factor have been proposed [6-10]. For polymer materials, the Arrhenius [9] and Williams-Landel-Ferry Equation (WLF) [10] equations are commonly used. For elastomers such as PSAs above the glass transition temperature, the shift factor  $a(\theta)$  follows the WLF equation, given by

$$\log_{10}a(\theta) = \frac{-d_1(\theta - \theta_r)}{d_2 + \theta - \theta_r} , \quad (10)$$

where  $d_1[-]$  and  $d_2[^\circ\text{C}]$  are constants. In order to identify the constants, we derived discrete values of the shift factor from stress relaxation experiments of an acrylic PSA. The Discrete values can be approximated with the WLF equation where  $d_1 = 12.2$  ,  $d_2 = 120[^\circ\text{C}]$  for  $\theta_r = 0[^\circ\text{C}]$ , as shown in Fig.3.

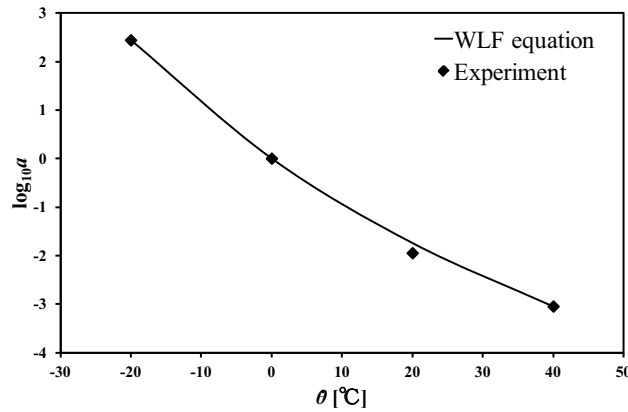


Figure 3. Time-temperature shift factor.

For the visco-hyperelastic formulation, we introduce Simo's finite-strain viscoelastic model [11]. The Cauchy stress tensor can be split into isochoric and volumetric parts, i.e.

$$\boldsymbol{\sigma} = \boldsymbol{\sigma}_{\text{iso}} + \boldsymbol{\sigma}_{\text{vol}} . \quad (11)$$

Here, the volumetric part  $\boldsymbol{\sigma}_{\text{vol}}$  is determined from the incompressibility constraint

$$J = \sqrt{\det \mathbf{B}} = 1 , \quad (12)$$

where  $J$  denotes the volume ratio. To readily enforce the incompressibility constraint within the context of finite element methods, near incompressibility is assumed, i.e.

$$\sigma_{\text{vol}} = \kappa(J - 1)\mathbf{I} \quad (13)$$

where  $\kappa$  is the penalty number. In this study, values of  $\kappa$  in the region of  $10^5 - 10^8$  are used for this purpose.

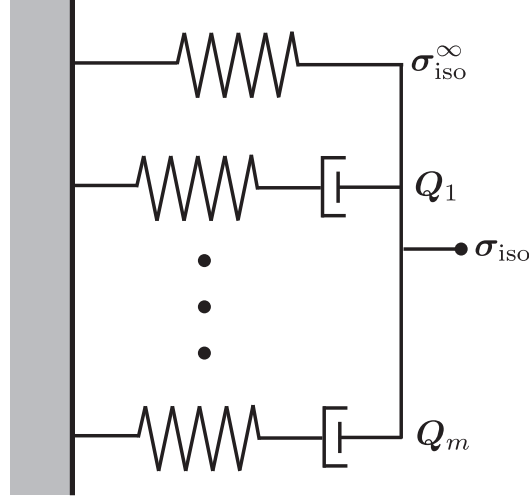


Figure 4. Generalized Maxwell model.

On the other hand, a time-dependent change of the system is caused purely by isochoric deformations. The isochoric part  $\sigma_{\text{iso}}$  is formulated with the generalized Maxwell model, shown in Fig.4. In this model, the isochoric part is given by

$$\sigma_{\text{iso}} = \sigma_{\text{iso}}^{\infty} + \sum_{\alpha=1}^m Q_{\alpha} , \quad (14)$$

$$\frac{DQ_{\alpha}}{Dt} = \frac{D\sigma_{\text{iso } \alpha}}{Dt} - \frac{Q_{\alpha}}{\tau'_{\alpha}} \quad (\alpha = 1, \dots, m) , \quad (15)$$

where  $\sigma_{\text{iso}}^{\infty}$  and  $\sigma_{\text{iso } \alpha}$  are the stress in the spring representing the hyperelasticity and  $Q_{\alpha}$  is the stress in the dashpot of the  $\alpha$ -Maxwell element characterizing the dissipation mechanism caused by the viscosity. In (15), the equivalent relaxation time  $\tau'$  at a reference temperature  $\theta_r$  is used to describe the temperature-dependence on the assumption that the temperature of PSAs is steady during deformations, i.e. the self-heating effects can be ignored. Simple closed form solutions of the evolution equations (15), which are valid for some semi-open time interval  $t \in (0, T]$ , are given by the convolution integrals

$$Q_{\alpha} = \exp\left(\frac{-T}{\tau'_{\alpha}}\right) Q_{\alpha}|_{t=0^+} + \int_{0^+}^T \frac{DQ_{\alpha}}{Dt} \exp\left\{\frac{-(T-t)}{\tau'_{\alpha}}\right\} dt \quad (16)$$

Let  $\Delta t$  be the time increment from time  $t^n$  to  $t^{n+1}$ , and then the numerical time integration algorithm of (16) is given by

$$Q_{\alpha}^{n+1} = \exp\left(\frac{-\Delta t}{\tau'_{\alpha}}\right) Q_{\alpha}^n + \exp\left(\frac{-\Delta t}{2\tau'_{\alpha}}\right) \beta_{\alpha}^{\infty} (\sigma_{\text{iso}}^{\infty n+1} - \sigma_{\text{iso}}^{\infty n}) , \quad (17)$$

where  $\beta_\alpha^\infty$  are non-dimensional constants defined by  $\sigma_{\text{iso } \alpha} = \beta_\alpha^\infty \sigma_{\text{iso}}^\infty$ .

The stress in the spring  $\sigma_{\text{iso}}^\infty$  is derived from the given strain-energy function  $\Psi_{\text{iso}}^\infty$ . Numerous specific forms of strain-energy functions have been proposed in the literature. For simulation-aided design of PSAs, the functional form should be simple and its physical meaning should be clear. Thus we focus on Yamashita-Kawabata strain-energy function [12]

$$\Psi_{\text{iso}}^\infty = c_1(\bar{I}_B - 3) + c_2(\bar{II}_B - 3) + \frac{c_3}{p+1}(\bar{I}_B - 3)^{p+1} \quad (18)$$

where  $c_1, c_2, c_3$ , and  $p (> 0)$  are constants.  $\bar{I}_B$  and  $\bar{II}_B$  are the modified invariants of the left Cauchy-Green deformation tensor and are defined by

$$\bar{I}_B = J^{-2/3} \text{tr} \mathbf{B} , \quad (19)$$

$$\bar{II}_B = J^{-4/3} \{ (\text{tr} \mathbf{B})^2 - \text{tr} (\mathbf{B}^2) \} . \quad (20)$$

Yamashita-Kawabata strain-energy function (18) was proposed for carbon-black filled rubbers. The first two terms and the third term on the right-hand-side of (18) represent the linear elastic and the hardening behaviors, respectively. Yamashita-Kawabata strain-energy function, however, cannot describe the stress-strain behavior of PSA with high accuracy because the stress-strain behavior of PSAs is more nonlinear than carbon-black filled rubbers. In this paper, therefore, we propose a novel strain-energy function based on Yamashita-Kawabata strain-energy function, i.e.

$$\Psi_{\text{iso}}^\infty = c_1(\bar{I}_B - 3) + c_2(\bar{II}_B - 3) + \frac{c_3}{p+1}(\bar{I}_B - 3)^{p+1} + \frac{c_4}{q+1}(\bar{II}_B - 3)^{q+1} \quad (21)$$

where  $c_1, c_2, c_3, c_4, p (> 0)$ , and  $q (> 0)$  are constants. The first two terms and the last two terms on the right-hand-side of (21) represent the linear elastic and the hardening behavior, respectively. To verify the advantages of the proposed strain-energy function (21), we compare computational results using the proposed strain-energy function (21) and Yamashita-Kawabata strain-energy function (18) in Section 4. The strain-energy functions (18)(21) give the most general form of a stress relation in terms of the modified invariants, which characterizes isotropic hyperelastic materials at finite strains, i.e.

$$\mathbf{S}_{\text{iso}}^\infty = 2 \frac{\partial \Psi_{\text{iso}}^\infty}{\partial \mathbf{C}} = 2 \left( \frac{\partial \Psi_{\text{iso}}^\infty}{\partial \bar{I}_C} \frac{\partial \bar{I}_C}{\partial \mathbf{C}} + \frac{\partial \Psi_{\text{iso}}^\infty}{\partial \bar{II}_C} \frac{\partial \bar{II}_C}{\partial \mathbf{C}} \right) , \quad (22)$$

where  $\bar{I}_B$  and  $\bar{II}_B$  are the modified invariants of the right Cauchy-Green deformation tensor and have the relationship

$$\bar{I}_C = \bar{I}_B , \quad (23)$$

$$\bar{II}_C = \bar{II}_B . \quad (24)$$

In (22) the derivatives of  $\bar{I}_C$  and  $\bar{II}_C$  with respect to  $\mathbf{C}$  are given [14] by

$$\frac{\partial \bar{I}_C}{\partial \mathbf{C}} = J^{-2/3} \left( \mathbf{I} - \frac{1}{3} I_C \mathbf{C}^{-1} \right) , \quad (25)$$

$$\frac{\partial \bar{II}_C}{\partial \mathbf{C}} = J^{-4/3} \left( I_C \mathbf{I} - \frac{2}{3} II_C \mathbf{C}^{-1} - \mathbf{C} \right) . \quad (26)$$

Substituting (25)(26) into (22), we obtain

$$\begin{aligned} \mathbf{S}_{\text{iso}}^{\infty} = & 2J^{-2/3} \left( \frac{\partial \Psi_{\text{iso}}^{\infty}}{\partial \bar{I}_C} + \frac{\partial \Psi_{\text{iso}}^{\infty}}{\partial \bar{II}_C} J^{-2/3} I_C \right) \mathbf{I} \\ & + 2J^{-2/3} \left( \frac{\partial \Psi_{\text{iso}}^{\infty}}{\partial \bar{II}_C} J^{-2/3} \right) \mathbf{C} - \frac{2}{3} J^{-2/3} \left( I_C \frac{\partial \Psi_{\text{iso}}^{\infty}}{\partial \bar{I}_C} + 2II_C \frac{\partial \Psi_{\text{iso}}^{\infty}}{\partial \bar{II}_C} J^{-2/3} \right) \mathbf{C}^{-1} \end{aligned} \quad (27)$$

(27) should be expressed in terms of not  $\mathbf{C}$  but  $\mathbf{B}$  because solid deformation is described with (8). Next, we introduce the Piola transformation [14]

$$\boldsymbol{\sigma}_{\text{iso}}^{\infty} = J^{-1} \mathbf{F} \cdot \mathbf{S}_{\text{iso}}^{\infty} \cdot \mathbf{F}^T . \quad (28)$$

With (27) we deduce from the Piola transformation (28) that

$$\begin{aligned} \boldsymbol{\sigma}_{\text{iso}}^{\infty} = & 2J^{-5/3} \left( \frac{\partial \Psi_{\text{iso}}^{\infty}}{\partial \bar{I}_B} + \frac{\partial \Psi_{\text{iso}}^{\infty}}{\partial \bar{II}_B} J^{-2/3} I_B \right) \mathbf{B} \\ & + 2J^{-5/3} \left( \frac{\partial \Psi_{\text{iso}}^{\infty}}{\partial \bar{II}_B} J^{-2/3} \right) \mathbf{B} \cdot \mathbf{B} - \frac{2}{3} J^{-5/3} \left( I_B \frac{\partial \Psi_{\text{iso}}^{\infty}}{\partial \bar{I}_B} + 2II_B \frac{\partial \Psi_{\text{iso}}^{\infty}}{\partial \bar{II}_B} J^{-2/3} \right) \mathbf{I} \end{aligned} \quad (29)$$

Rearranging (29) with the modified invariants (19)(20) and the modified left Cauchy-Green deformation tensor, defined by

$$\bar{\mathbf{B}} = J^{-2/3} \mathbf{B} , \quad (30)$$

we finally obtain

$$\boldsymbol{\sigma}_{\text{iso}}^{\infty} = \frac{2}{J} \left\{ \left( \frac{\partial \Psi_{\text{iso}}^{\infty}}{\partial \bar{I}_B} + \frac{\partial \Psi_{\text{iso}}^{\infty}}{\partial \bar{II}_B} \bar{I}_B \right) \bar{\mathbf{B}} + \frac{\partial \Psi_{\text{iso}}^{\infty}}{\partial \bar{II}_B} \bar{\mathbf{B}} \cdot \bar{\mathbf{B}} - \frac{1}{3} \left( \bar{I}_B \frac{\partial \Psi_{\text{iso}}^{\infty}}{\partial \bar{I}_B} + 2\bar{II}_B \frac{\partial \Psi_{\text{iso}}^{\infty}}{\partial \bar{II}_B} \right) \mathbf{I} \right\} . \quad (31)$$

### 3. EULERIAN FINITE ELEMENT FORMULATION

In this section, the numerical algorithm for solving the basic equations is presented in terms of an Eulerian/ALE finite element method [5, 15]. The Eulerian/ALE formulation in this study is based on an operator splitting strategy for breaking complicated equations into a series of less complicated equations [13].

#### 3.1. Operator splitting

The basic equations have the general conservation form

$$\frac{\partial \Phi}{\partial t} + \mathbf{c} \cdot \nabla \Phi = \mathbf{S} , \quad (32)$$

where  $\Phi$  is the arbitrary function,  $\mathbf{c}$  is the relative velocity between the material and the mesh, and  $\mathbf{S}$  is the source term. The relative velocity  $\mathbf{c}$  is defined by

$$\mathbf{c} = \mathbf{v} - \hat{\mathbf{v}} , \quad (33)$$

where  $\hat{\mathbf{v}}$  is the mesh velocity. If the mesh velocity is null, (32) reduces to a Eulerian equation. If, on the other hand, the mesh velocity is not null, (32) is an arbitrary Lagrangian-Eulerian

(ALE) equation. In this study, the ALE formulation is used to impose the kinematic and dynamic boundary conditions (2)(3) on material interfaces. That's because the present Eulerian formulation cannot deal with them due to dissipated interfaces.

Operator splitting divides (32) into two equations,

$$\frac{\partial \Phi}{\partial t} = \mathbf{S} , \quad (34)$$

$$\frac{\partial \Phi^*}{\partial t} + \mathbf{c} \cdot \nabla \Phi^* = 0 , \quad (35)$$

which are then solved sequentially. (34), the non-advective step, contains the source term, and (35), the advective step, contains the convective term. A superscript \* of (35) shows the variable after the non-advective step. Fig.5 illustrates the steps in the Eulerian/ALE formulation. The difference between (34) and the standard Lagrangian equations is the type of the time derivative. (34) is hence identical to the standard Lagrangian formulation if the spatial time derivative is replaced by the material time derivative. To solve (35), the deformed mesh is moved to the fixed Eulerian mesh or the relaxed ALE mesh, and volume fraction of material transported between adjacent elements is calculated. The Lagrangian solution variables such as the velocity vector, Cauchy stress tensor and left Cauchy-Green deformation tensor are then adjusted to account for the flow of the material between adjacent elements by the transport algorithms presented below.

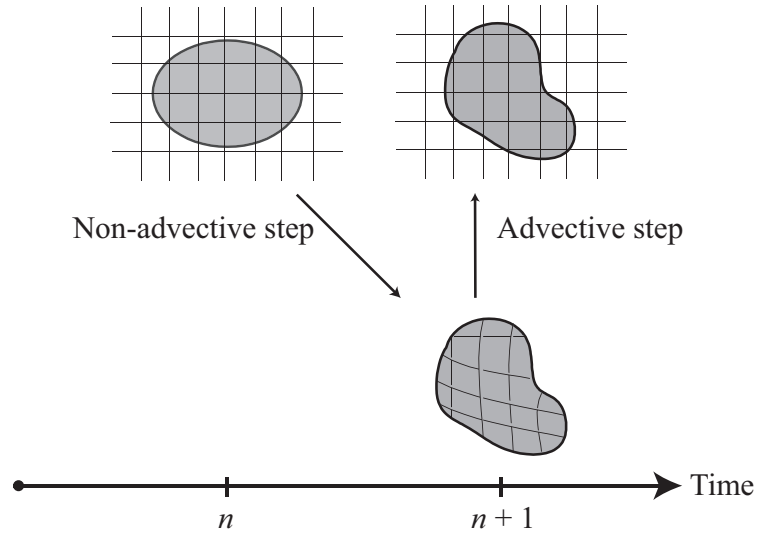


Figure 5. The operator split for Eulerian/ALE formulation.

### 3.2. Non-advective step

The virtual work equation is derived from the non-advective part of (1),

$$\int_{\Omega} \rho \mathbf{a} \cdot \delta \mathbf{u} dV + \int_v \boldsymbol{\sigma} : (\delta \mathbf{u} \otimes \nabla) dV = \int_{\Gamma_t} \bar{\mathbf{t}} \cdot \delta \mathbf{u} dS + \int_{\Omega} \rho \mathbf{b} \cdot \delta \mathbf{u} dV \quad (36)$$

where  $\delta \mathbf{u}$  is the virtual displacement vector and  $\mathbf{a}$  is the acceleration vector. The updated Lagrangian formulation is used since the reference configuration is the current configuration



in the Eulerian/ALE formulation. To avoid volumetric locking, selective reduced integration [16] is used for the spatial discretization. The discrete equation of (36) is

$$\mathbf{M}\hat{\mathbf{a}} + \mathbf{F}_{\text{int}} = \mathbf{F}_{\text{ext}} \quad (37)$$

where  $\hat{\mathbf{a}}$  is the nodal acceleration vector,  $\mathbf{M}$  is the mass matrix, and  $\mathbf{F}_{\text{int}}$  and  $\mathbf{F}_{\text{ext}}$  are the internal and external force vectors, respectively. These matrices and vectors are given by

$$\mathbf{M} = \sum_{e=1}^{N_{\text{el}}} \rho \int_{\Omega_e} \mathbf{N}^T \mathbf{N} dV_e, \quad (38)$$

$$\mathbf{F}_{\text{int}} = \sum_{e=1}^{N_{\text{el}}} \int_{\Omega_e} \mathbf{B}_{\text{sd}}^T \boldsymbol{\sigma} dV_e, \quad (39)$$

$$\mathbf{F}_{\text{ext}} = \sum_{e=1}^{N_t} \int_{\Gamma_t} \mathbf{N}^T \bar{\mathbf{t}} dS_e + \sum_{e=1}^{N_{\text{el}}} \int_{\Omega_e} \rho \mathbf{N}^T \mathbf{b} dV_e, \quad (40)$$

where  $\mathbf{N}$  is the shape function matrix, and  $\mathbf{B}_{\text{sd}}$  represents the strain-displacement matrix. In addition,  $N_{\text{el}}$  is the number of total elements, while  $N_t$  and  $N_{\text{el}}$  are the numbers of elements whose edges are adjacent to the kinematic and dynamic boundaries, respectively.

The explicit formulation advances the solution in time with the central difference method,

$$\hat{\mathbf{a}}^n = \overline{\mathbf{M}}^{-1} (\mathbf{F}_{\text{ext}}^n - \mathbf{F}_{\text{int}}^n), \quad (41)$$

$$\hat{\mathbf{v}}^{n+1/2} = \hat{\mathbf{v}}^{n-1/2} + \Delta t \hat{\mathbf{a}}^n, \quad (42)$$

$$\hat{\mathbf{x}}^{n+1} = \hat{\mathbf{x}}^n + \Delta t \hat{\mathbf{v}}^{n+1/2}, \quad (43)$$

where  $\overline{\mathbf{M}}$  is the diagonal lumped mass matrix transformed from the consistent mass matrix (38),  $\hat{\mathbf{a}}$  is the nodal velocity vector, and  $\hat{\mathbf{x}}$  is the nodal position vector. After calculating the nodal velocity vector, the left Cauchy-Green deformation tensor and the Cauchy stress tensor are updated. The explicit formulation of the non-advective part of (8) is given by

$$\mathbf{L}^{n+1/2} = \mathbf{B}_{\text{sd}}^{n+1/2} \hat{\mathbf{v}}^{n+1/2}, \quad (44)$$

$$\mathbf{B}^{n+1} = \mathbf{B}^n + \Delta t \{ \mathbf{L}^{n+1/2} \cdot \mathbf{B}^n + \mathbf{B}^n \cdot (\mathbf{L}^T)^{n+1/2} \}. \quad (45)$$

### 3.3. Advective step

In the advective step, the velocity, Cauchy stress, and left Cauchy-Green deformation tensor are remapped from the Lagrangian mesh onto the fixed Eulerian mesh or the relaxed ALE mesh with the second-order MUSCL scheme [17]. The advective calculation is further split into a sequence of one-dimensional advection steps. The spatial locations of the material boundaries is also advected by solving the advection equation of Volume-Of-Fluid (VOF) function [18]. To avoid the numerical instability brought by the numerical diffusion in the void domain, we update the left Cauchy-Green deformation tensor with VOF function  $\phi$ :

$$\tilde{\mathbf{B}}^{n+1} = \begin{cases} \mathbf{B}^{n+1} & \text{for } \phi^{n+1} \geq \phi_{\min} \\ \mathbf{0} & \text{for } \phi^{n+1} < \phi_{\min} \end{cases} \quad (46)$$

where  $\phi_{\min}$  is a threshold. In this study, values of  $\phi_{\min}$  in the region of  $10^{-2} - 10^{-1}$  are used.

#### 4. NUMERICAL EXAMPLES

To validate the proposed approach, we compare the computational and experimental results of uniaxial tension tests under different tensile speed and temperature conditions. Fig.6 is the computational model in two dimensions for uniaxial tension tests. The domain is discretized with  $33 \times 50$  mesh of uniform square elements. Values for the material constants for Yamashita-Kawabata strain-energy function (18) and those for our proposed strain-energy function are given in Tables 1 and 2, respectively. These were experimentally obtained from uniaxial tension tests. All the walls are assumed not to have friction, and the symmetry condition is imposed along the left edge of the PSA. The constant velocity in the vertical upward direction is imposed on the top surface of the PSA, and then the ALE finite element method is selected in order to enforce this boundary condition.

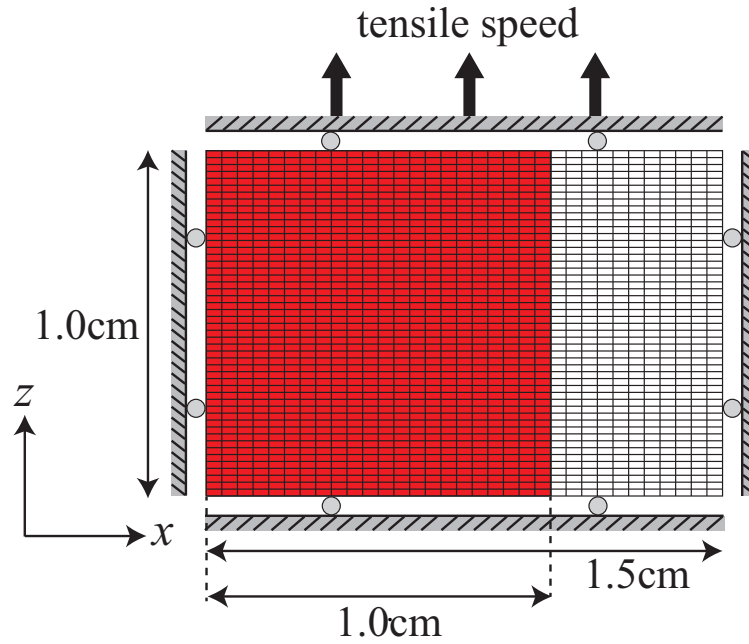


Figure 6. Computational model of uniaxial tension.

The first validation experiment considered is an uniaxial tensile test at different tensile speeds (500mm/min, 50mm/min, 5mm/min) and constant temperature (20°C). The numerical accuracy is quantified by the error

$$\varepsilon = \frac{1}{N_d} \sum_{i=1}^{N_d} \frac{|\sigma_i^{\text{exp.}} - \sigma_i^{\text{comp.}}|}{\sigma_i^{\text{exp.}}}, \quad (47)$$

where  $N_d$  is the amount of experimental data,  $\sigma$  is the  $zz$  component of the Cauchy stress tensor  $\boldsymbol{\sigma}$ . Fig.7 (with Yamashita-Kawabata strain-energy function) and Fig.8 (with our proposed strain-energy function) show comparison between the experimental and the computational results. Our proposed strain-energy function enables us to reduce the error rate by 78.6% thus giving a more accurate description of the visco-hyperelastic behavior of PSAs.

In the second validation experiment, we also compare the experimental and computational results using first Yamashita-Kawabata strain-energy function in Fig.9 and then our

proposed strain-energy function in Fig.10. However, in this uniaxial tension test, we consider constant tensile speed (50mm/min) at different temperature (0°C, 20°C, 40°C) conditions. The improvement in accuracy of description of the temperature-dependent behavior of PSAs is 32.7% compared with the calculation that employed Yamashita-Kawabata strain-energy function. However, the computation at 0°C, shown in Fig.10, doesn't show good qualitative agreement with experimental data. This is probably due to the low accuracy of the shift factor measurement in the low temperature regime.

Finally, we check whether the material volume is numerically conserved during the simulation because incompressible materials keep the volume constant throughout a motion. Fig.11 shows the deformation at nominal strain of 0% and 1000%. The material volume is well conserved during the simulation with error under 1.4%.

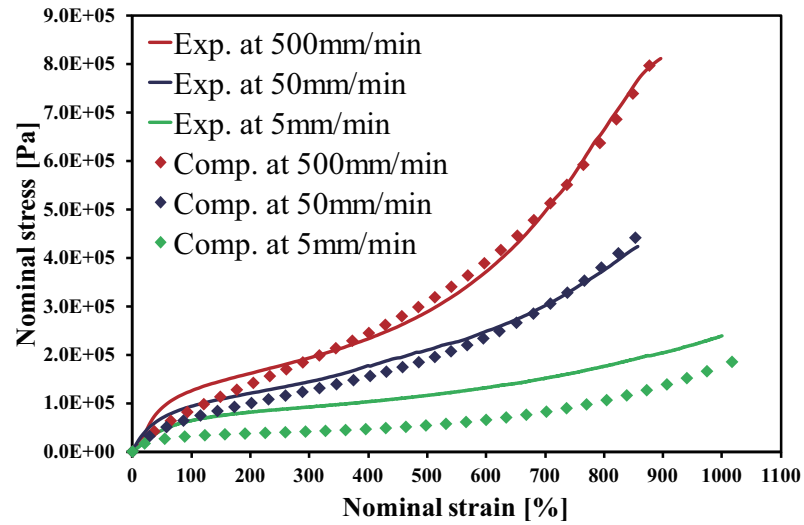


Figure 7. Comparison between the experimental and computational results of uniaxial tension tests at a constant temperature (20°C) with Yamashita-Kawabata strain-energy function.

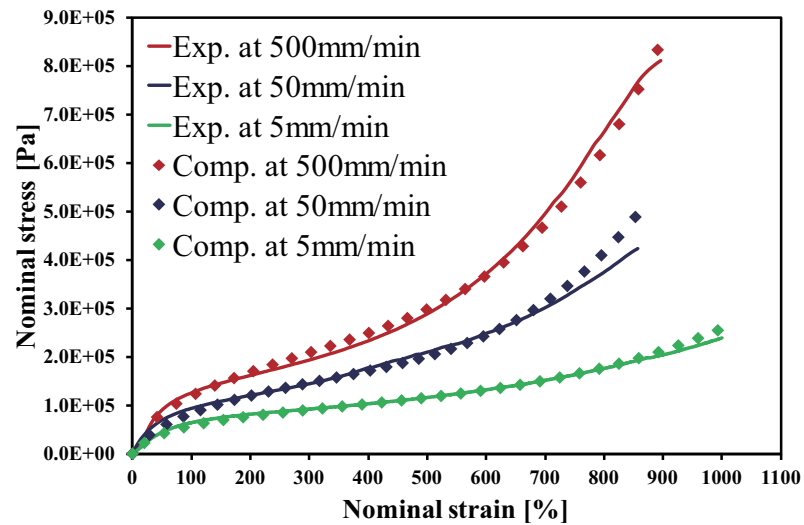


Figure 8. Comparison between the experimental and computational results of uniaxial tension tests at a constant temperature (20°C) with our proposed strain-energy function.

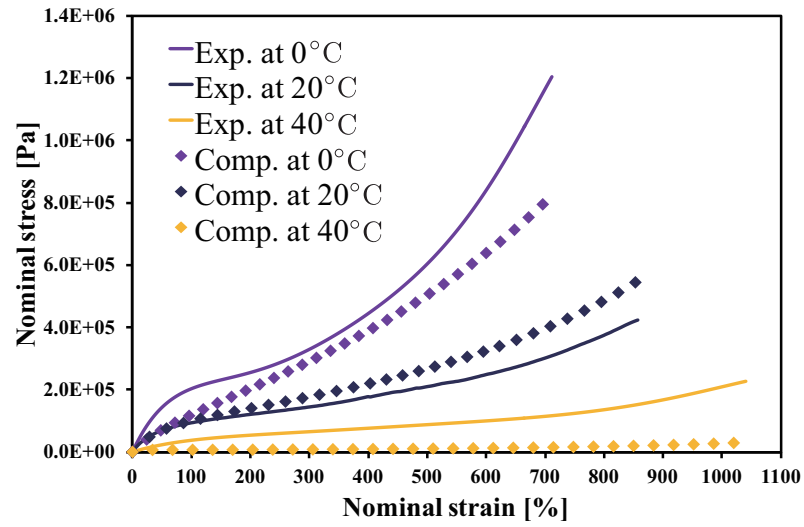


Figure 9. Comparison between the experimental and computational results of uniaxial tension tests at a constant tensile speed (50mm/min) with Yamashita-Kawabata strain-energy function.

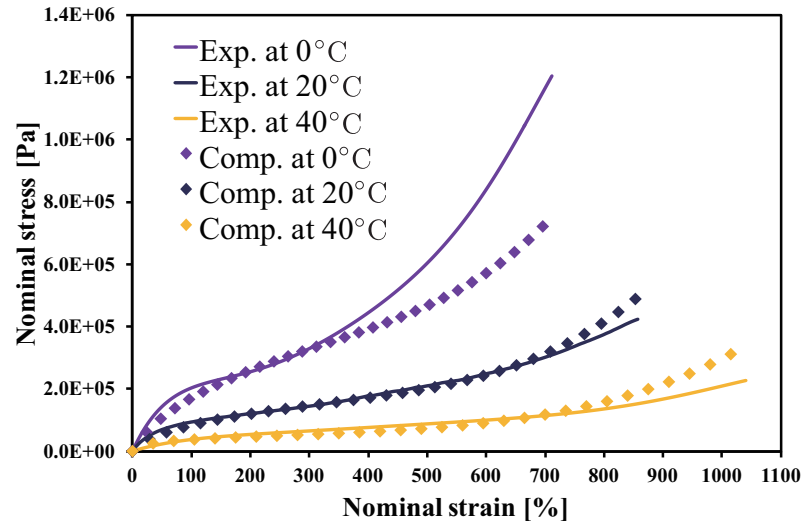


Figure 10. Comparison between the experimental and computational results of uniaxial tension tests at a constant tensile speed (50mm/min) with our proposed strain-energy function.

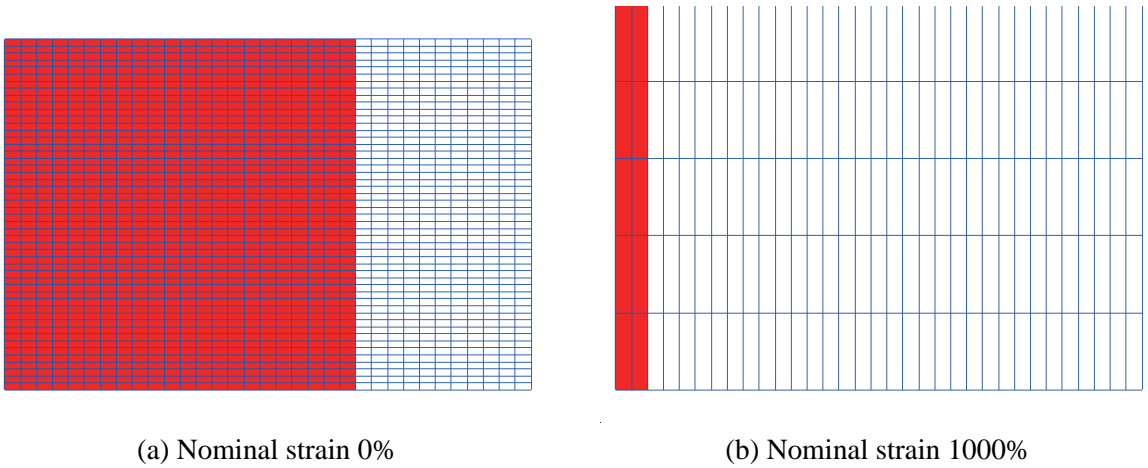


Figure 11. Deformation simulated with the ALE finite element method.

Table 1. Values of the material constants for Yamashita-Kawabata strain-energy function.

hyperelastic parameters			
$c_1$ [Pa]	$2.32 \times 10^1$		
$c_2$ [Pa]	$1.00 \times 10^{-5}$		
$c_3$ [Pa]	$6.80 \times 10^{-3}$		
$p$ [-]	1.76		

viscous parameters			
$\beta_1^\infty$ [-]	1.00	$\tau_1$ [s]	1.00
$\beta_2^\infty$ [-]	$5.19 \times 10^2$	$\tau_2$ [s]	$1.00 \times 10^1$
$\beta_3^\infty$ [-]	1.00	$\tau_3$ [s]	$5.00 \times 10^1$
$\beta_4^\infty$ [-]	$5.62 \times 10^2$	$\tau_4$ [s]	$1.00 \times 10^2$
$\beta_5^\infty$ [-]	1.00	$\tau_5$ [s]	$1.00 \times 10^3$

temperature-dependent parameters	
$d_1$ [-]	12.2
$d_2$ [°C]	120.0
$\theta_s$ [°C]	0

Table 2. Values of the material constants for our proposed strain-energy function.

hyperelastic parameters			
$c_1$ [Pa]	$5.00 \times 10^3$		
$c_2$ [Pa]	$-2.89 \times 10^1$		
$c_3$ [Pa]	$4.88 \times 10^{-1}$		
$c_4$ [Pa]	1.60		
$p$ [-]	$4.19 \times 10^{-7}$		
$q$ [-]	1.15		

viscous parameters			
$\beta_1^\infty$ [-]	1.00	$\tau_1$ [s]	$1.00 \times 10^{-5}$
$\beta_2^\infty$ [-]	1.00	$\tau_2$ [s]	$1.00 \times 10^{-5}$
$\beta_3^\infty$ [-]	1.10	$\tau_3$ [s]	$1.00 \times 10^{-5}$
$\beta_4^\infty$ [-]	5.40	$\tau_4$ [s]	$4.00 \times 10^{-1}$
$\beta_5^\infty$ [-]	1.70	$\tau_5$ [s]	$1.70 \times 10^1$
$\beta_6^\infty$ [-]	2.70	$\tau_6$ [s]	$1.00 \times 10^2$

temperature-dependent parameters	
$d_1$ [-]	12.2
$d_2$ [°C]	120.0
$\theta_s$ [°C]	0

## 5. CONCLUSIONS

In this paper, we proposed the temperature-dependent visco-hyperelastic formulation based on an Eulerian finite element method for the dynamics of PSAs. All the basic equations were numerically solved in the Eulerian/ALE framework because it allows arbitrarily large deformations. Visco-hyperelasticity was formulated using Simo's finite-strain viscoelastic model, where hyperelasticity was modeled as our proposed strain energy function of the left Cauchy-Green deformation tensor. The left Cauchy-Green deformation tensor was temporally updated from the Eulerian velocity field without material points. Temperature-dependence was described with the time-temperature superposition principle of Williams, Landel, and Ferry. To validate the proposed approach, we simulated uniaxial tension tests under different tensile speed and temperature conditions. Our proposed scheme gave quantitative description of the visco-hyperelastic and temperature-dependent behaviour of PSAs even in the large strain regime.

The significance of the present Eulerian formulation is that in addition to application of this approach to large deformation analysis of PSAs it can be used in large deformation analysis of amorphous polymer materials that have visco-hyperelasticity and temperature-dependence. Moreover, the present Eulerian formulation is well-suited for application of the voxel-based multi-component geometry in the spatially-fixed mesh. Once the initial field of the solid volume fraction is given by X-ray CT system, the present Eulerian method enables us to treat complex surface shapes or internal structures with ease because mesh generation procedure is not necessary. The practical demonstration is the subject of our future study.

## 6. REFERENCES

- [1] Y. Urahama, "Effect of peel load on stringiness phenomena and peel speed of pressure-sensitive adhesive tape", *The Journal of Adhesion*, 31, 47-58, 1989.
- [2] A. Zosel, "Adhesive failure and deformation behavior of polymers", *The Journal of Adhesion*, 30, 135-149, 1989.
- [3] D. Satas, *Handbook Of Pressure Sensitive Adhesive Technology*, Springer, 1989.
- [4] K. Nishiguchi, K. Maeda, S. Okazawa, S. Tanaka, "A visco-hyperelastic analysis scheme by using a full Eulerian finite element method for dynamics of pressure-sensitive adhesives", *Transactions of The Japan Society of Mechanical Engineers Series A*, accepted, 2012 (in Japanese).
- [5] D. J. Benson, "Computational methods in Lagrangian and Eulerian hydrocodes", *Computer Methods in Applied Mechanics and Engineering*, 99, 235-394, 1992.
- [6] H. Smith, *Elastic and creep properties of filamentous materials and other high polymers*, The Textile Foundation in Washington, 1944.
- [7] J. D. Ferry, "Mechanical properties of substances of high molecular weight. VI. dispersion in concentrated polymer Solutions and its Dependence on Temperature and Concentration", *J. Am. Chem. Soc.*, 72, 3746-3752, 1950.
- [8] F. Schwarzl, A. J. Staverman, "Time temperature dependence of linear viscoelastic behavior", *Journal of Applied Physics*, 23, 838-843, 1952.

- [9] S. Glasstone, J. Laidler, H. Eyring, *The Theory of Rate Processes* (first edition), McGraw-Hill Book Company, 1941.
- [10] M. L. Williams, R. F. Landel, J. D. Ferry, "The temperature dependence of relaxation mechanisms in amorphous polymers and other glass-forming liquids", *J. Am. Chem. Soc.*, 77, 3701-3707, 1955.
- [11] J. C. Simo, "On a fully three dimensional finite strain viscoelastic damage model: formulation and computational aspects", *Computer Methods in Applied Mechanics and Engineering*, 60, 153-173, 1987.
- [12] Y. Yamashita, S. Kawabata, "Approximated form of the strain energy-density function of carbon-black filled rubbers for industrial applications", *Journal of the Society of rubber Industry*, 65, 517-528, 1992 (in Japanese).
- [13] A. J. Chorin, T. J. R. Hughes, M. F. McCracken, J. E. Marsden, "Product formulas and numerical algorithms", *Communications on Pure and Applied Mathematics*, 31, 205-256, 1978.
- [14] G. A. Holzapfel, *Nonlinear solid mechanics / a continuum approach for engineering*, 205-256, John Wiley and Sons, 2000.
- [15] J. Donea, S. Giuliani, J. P. Halleux, "An Arbitrary Lagrangian-Eulerian finite element method for transient dynamic fluid-structure interactions", *Comput. Meth. Appl. Mech. Eng.*, 33, 689-723, 1982.
- [16] T. J. R. Hughes, "Generalization of selective integration procedures to anisotropic and nonlinear media", *International Journal for Numerical Methods in Engineering*, 15, 1413-1418, 1980.
- [17] B. Van Leer, "Towards the ultimate conservative difference scheme IV: A new approach to numerical convection", *Journal of Computational Physics*, 23, 276-299, 1977.
- [18] C. W. Hirt, B. D. Nichols, "Volume of fluid (VOF) method for the dynamics of free boundaries", *Journal of Computational Physics*, 39, 201-225, 1981.